ENGINEERING

Liquid-bodied antibiofilm robot with switchable viscoelastic response for biofilm eradication on complex surface topographies

Bonan Sun[1], Junjia Guo[2], Bo Hao[1], Yanfei Cao[1], Tony K. F. Chan[3], Mengmeng Sun[4]*, Joseph J. Y. Sung[5]*, Li Zhang[1,3,6,7,8]*

Recalcitrant biofilm infections pose a great challenge to human health. Micro- and nanorobots have been used to eliminate biofilm infections in hard-to-reach regions inside the body. However, applying antibiofilm robots under physiological conditions is limited by the conflicting demands of accessibility and driving force. Here, we introduce a liquid-bodied antibiofilm robot constructed by a dynamically cross-linked magnetic hydrogel. Leveraging the viscoelastic response of the robot enables it to adapt to complex surface topographies such as medical meshes and stents. Upon actuation, the robot can mechanically destroy the biofilm matrix, chemically deactivate bacterial cells, and collect disrupted biofilm debris. The robot's antibiofilm performance is studied in vitro and demonstrated on a medical mesh and a biliary stent. Tracking and navigation under endoscopy and x-ray imaging in an ex vivo porcine bile duct are demonstrated. Last, in vivo antibiofilm treatment is conducted by indwelling infected stents into mice's abdominal cavity and clearing the biofilm infection using the proposed robot.

INTRODUCTION

Persistent microbial infections present a major threat to public health, causing approximately 4.95 million deaths in 2019 (*1*). Although pathogenic microbes are commonly thought of as planktonic bacteria with flagellar tails, most live within dynamic, self-assembled structures known as biofilms. Roughly 80% of chronic infections are recognized as biofilm infections (*2*, *3*). Initially, planktonic bacteria adhere to a surface of human tissue or implant, then aggregate with other microbes and produce adherent extracellular polymeric substances (EPS) to form a biofilm (*4*, *5*). The EPS matrix, consisting of polysaccharides, fibrous proteins, and extracellular DNA, protects the hosting microbes against environmental stresses and antibiotics, making biofilm infections difficult to eliminate inside the human body (*6*–*8*). While both biotic and abiotic surfaces can be colonized by biofilms, abiotic implants such as medical meshes, stents, and catheters are particularly susceptible to biofilm infection due to suppressed immune responses in their vicinity (*9*). Generally, there are two treatments for implant-associated biofilm infections: (i) physical removal of biofilm or replacement of the infected device, necessitating invasive surgery to access the infected implant; and (ii) antibiotic chemotherapy is hindered by low local concentration and the inability to penetrate the biofilm matrix and eradicate the infection. Moreover, the overuse of antibiotics has caused rising antimicrobial resistance and even the emergence of superbugs that are resistant to most available antibiotics (*1*, *7*).

To eliminate recalcitrant biofilm infections inside the body, micro-/nanorobots (MNRs) have emerged as a promising tool. MNRs are small-scale machines fabricated to perform designated tasks in hard-to-reach regions (*10*–*13*). MNRs offer minimally invasive medical interventions due to their small size (*14*–*17*), and they can be driven by external physical fields [e.g., magnetic (*18*), ultrasound (*19*), or light (*20*)] to navigate inside the body and perform targeted therapy (*21*–*24*). Recently, MNRs have been used for antibiofilm applications (*25*–*29*). Reported antibiofilm MNRs can eliminate established biofilms in vitro under the actuation of external fields through diverse mechanisms. Among them, chemical-mechanical disruption of the biofilm matrix is the most common approach (*25*). For instance, microswarms consisting of iron oxide nanoparticles can mechanically disrupt the biofilm matrix while generating free radicals that chemically dissolve the biofilm matrix and eliminate bacterial cells (*30*–*32*); catalytic micromotors decompose hydrogen peroxide solution and produce free radicals while moving randomly driving by microbubbles (*33*–*36*). However, these antibiofilm robots alone cannot function inside the body; they rely on the injection of hydrogen peroxide into the biofilm site to provide "fuel" for their antibiofilm functionalities. As an improvement, antibiofilm MNRs loaded with antimicrobial agents have been designed. A thermosensitive magnetic hydrogel micromachine absorbs hydrogen peroxide solution and releases it upon triggering, showing the capability to eradicate biofilms in tubular catheters without injection of antimicrobial agents (*37*). Alternatively, antibiotics or antimicrobial peptides can be bonded to microrobots through chemical modification and delivered to the biofilm site (*38*, *39*).

Although diverse MNRs show antibiofilm capability in vitro, few have been tested under in vivo conditions. Attempts have been made to integrate antibiofilm MNRs with medical imaging modalities toward a microrobotic surgery platform. For example, a magnetic helical micromachine was used to eradicate biofilm in a tympanostomy tube, a tubular implant in the human ear canal (*40*). In addition, a magnetic microswarm featuring urchin-like structures was used to eradicate biofilm in a plastic biliary stent (*41*). Endoscopy was used in the aforementioned two works to deliver the antibiofilm robots into

[1]Department of Mechanical and Automation Engineering, The Chinese University of Hong Kong, Hong Kong SAR, China. [2]Department of Biomedical Engineering, The Chinese University of Hong Kong, Hong Kong SAR, China. [3]Chow Yuk Ho Technology Center for Innovative Medicine, The Chinese University of Hong Kong, Hong Kong SAR, China. [4]Physical Intelligence Department, Max Planck Institute for Intelligent Systems, 70569 Stuttgart, Germany. [5]Lee Kong Chian School of Medicine, Nanyang Technological University, Singapore, Singapore. [6]Multi-Scale Medical Robotics Center, Hong Kong Science Park, Hong Kong SAR, China. [7]Department of Surgery, The Chinese University of Hong Kong, Hong Kong SAR, China. [8]CUHK T. Stone Robotics Institute, The Chinese University of Hong Kong, Hong Kong SAR, China.
*Corresponding author. Email: mmttsun@outlook.com (M.S.); josephsung@ntu.edu.sg (J.J.Y.S.); lizhang@cuhk.edu.hk (L.Z.)

the biofilm site and track their movement, and the platform's efficacy was demonstrated in ex vivo surgeries. However, a major hindrance to in vivo application is the limited adaptability of the antibiofilm robots. Current robots cannot eradicate biofilms on medical implants with complex topographic features, such as meshes and metallic stents. Examples of medical implants' topographical complexity are summarized in table S1 (text S1). Specifically, two crucial features are needed for antibiofilm MNRs to work on complex topographies: (i) They should be able to access narrow trenches and deep crevices to clear biofilm within, which demands small size or large deformability, and (ii) they have to move in viscous biofilm secretions and translate through liquid-gas interfaces, which requires a large driving force for these robots. Most reported micro-/nanoparticle collectives ("microswarm") or micromotors satisfy the first requirement due to their small size but fail to meet the second. Antibiofilm robots with larger sizes, such as the millimeter-sized magnetic hydrogel micromachine (*37*) and the rod-like robot (*42*), have sufficient driving force for translating liquid-gas interfaces but fail to access narrow regions as their deformability is limited. The conflict between small size and large driving force for MNRs stems from a basic physical principle—scaling law—and it seems that it has not been adequately addressed (*43*).

To provide a potential solution for the conflict between accessibility and driving force, we propose a liquid-bodied antibiofilm robot. The proposed robot comprises a magnetic hydrogel cross-linked by dynamic boronic ester bonds, which provide exceptional deformation and instantaneous self-healing capabilities (*44*, *45*). Embedded with NdFeB microparticles, the antibiofilm robot responds to external magnetic fields. Figure 1A illustrates the switchable viscoelastic response of the robot triggered by magnetic actuation: under gradient magnetic fields, the robot deforms slowly and moves on a substrate; under rotating magnetic fields, the robot flips with the external fields, showing a rolling motion. The dual-modal response is governed by two characteristic timescales: actuation time Γ and relaxation time τ. When Γ is less than τ, the robot shows an elastic deformation response, and when Γ is greater than τ, the robot shows a viscous liquid–like response. We can switch between two modes of response by manipulating the applied magnetic field parameters. The dual-modal response is essential for the antibiofilm treatment on complex topographies such as medical meshes and metallic stents. As an example, we illustrate the biofilm infection on a metallic biliary stent in Fig. 1B: The soft bile duct is supported by the metallic stent, creating undulating surfaces that are difficult to overcome for miniature robots. In contrast, the proposed antibiofilm robot crosses over undulating surfaces under rotating magnetic fields and conforms to the deep crevices to clear biofilm within under gradient magnetic fields. We illustrate the antibiofilm mechanisms of the proposed robot in Fig. 1C: The robot mechanically disrupts the biofilm matrix through its movement driven by external fields while actively releasing antimicrobial agents to kill the bacteria cells. The synergistic effect combining mechanical and chemical disruption of the biofilm matrix enhances the effectiveness of biofilm eradication. Meanwhile, the boronic acid–diol interaction between the robot and the biofilm matrix polysaccharides enables the collection and removal of biofilm debris, preventing the dispersal and regrowth of disrupted biofilm fragments. Last, Fig. 1D shows the microrobotic surgery platform for a medical imaging–guided antibiofilm treatment using the proposed robot. The antibiofilm robot is delivered to the biofilm site through endoscopy and tracked by x-ray fluoroscopy. Magnetic actuation of the robot is achieved by programming the moving trajectory of a permanent magnet integrated with a motor and a robotic arm. Using the proposed system, imaging and tracking of the antibiofilm robot in an ex vivo porcine bile duct are demonstrated. Last, to assess the robot's antibiofilm performance in vivo, we implant infected stents into mice's abdominal cavity and deliver the robot for antibiofilm treatment. The proposed antibiofilm robot is capable of eliminating biofilms on complex surface topographies and thus has great potential for clinical treatments of a wide range of implant-associated biofilm infections.

RESULTS

Characterization, locomotion, and mechanical biofilm removal

The proposed antibiofilm robot comprises a dynamically cross-linked polyvinyl alcohol (PVA) hydrogel with embedded magnetic particles. The PVA chains feature an abundance of hydroxyl groups, facilitating cross-linking through boronic acids to form boronic ester bonds (*44*, *46*, *47*). Notably, these dynamic boronic ester bonds form and debond under room temperature conditions without the need for catalysts or external stimuli (*45*, *48*). A slime-like viscoelastic hydrogel can be obtained immediately after mixing PVA and borate solution (fig. S1A). Antimicrobial agent levofloxacin and indolicidin are loaded within the hydrogel matrix, and their chemical structures are shown in fig. S1B. Frequency sweeps are conducted to investigate the rheological behaviors of the magnetic hydrogels. All measured formulations show strong rate-dependent behaviors, where the storage modulus (G') varies in a range of five to six orders of magnitudes under different shear rates (Fig. 2A and fig. S2). Shear-thickening behavior is observed, where the storage modulus is lower than the loss modulus (G'') at low shear rates but higher at high shear rates. The viscoelastic response can be triggered by applying external magnetic fields. Under magnetic actuation, the force and torque exerted on the material can be expressed as $\mathbf{f_m} = (\mathbf{m} \cdot \nabla)\mathbf{B}$ and $\boldsymbol{\tau}_\mathbf{m} = \mathbf{m} \times \mathbf{B}$, where $\mathbf{f_m}$, $\boldsymbol{\tau}_\mathbf{m}$, $\mathbf{m}$, and $\mathbf{B}$ denote magnetic force and torque, magnetic moment, and magnetic field, respectively (*49*). In magnetic soft materials, only the magnetic particle phase experiences magnetic force and torque, while the polymeric matrix phase is nonmagnetic. The magnetic particles are embedded and restrained in the polymer matrix. Consequently, the magnetic force and torque are transferred from the magnetic particles to the matrix, resulting in elastic deformation of the body (*50*). However, the magnetic hydrogels cross-linked by dynamic covalent bonds only demonstrate elastic response under high shear rates. As the phase diagram depicts in Fig. 2B, an elastic response similar to reported hard-magnetic soft materials can be observed under strong magnetic fields (denoted by normalized magnetic field strength MB/G, where M is the magnetization of the robot, B is magnetic flux density, and G is the shear modulus of the robot) and high rotating frequencies of the magnetic field; under weak magnetic fields and low frequencies, bond exchange reaction prevails, and the robot shows liquid-like viscous response while the dynamic bonds are readily cleaved and reformed (fig. S3) (*45*, *51*). The product of the two quantities yields an actuation timescale, $\Gamma = G/fMB$, which can be compared with the intrinsic relaxation time of the material, τ_r, to determine which response will dominate under given actuation parameters (text S2). We put a nonmagnetic brass screw on the top of the magnetic hydrogel robot (Fig. 2C). Without applying a magnetic field, the screw sinks into the viscous hydrogel in 4 min. However, under a rotating magnetic field ($f = 3$, $MB/G = 0.1$), the hydrogel hardens and supports the screw

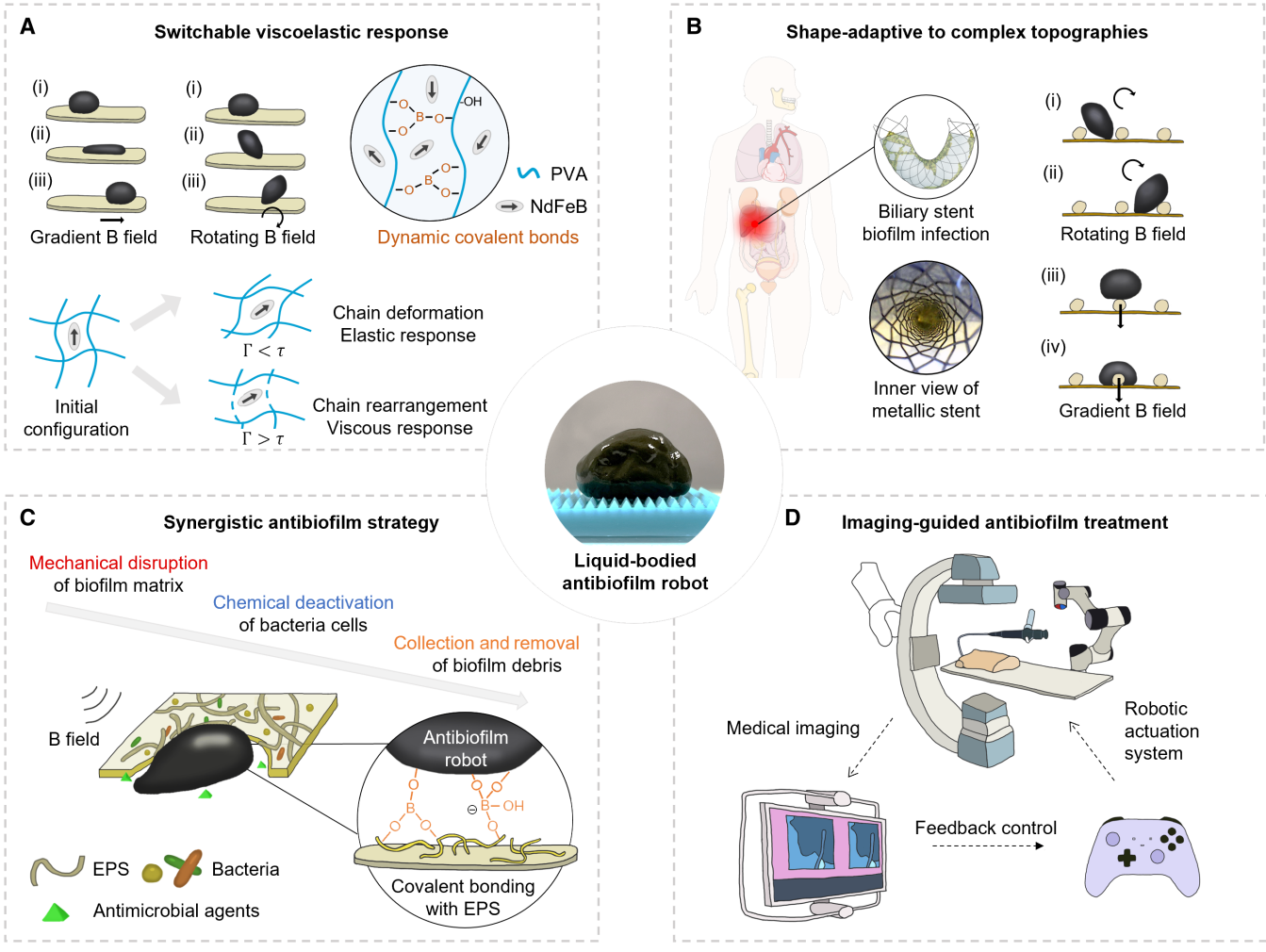

Fig. 1. Schematics of the liquid-bodied antibiofilm robot. (**A**) The switchable viscoelastic response of the antibiofilm robot can be triggered by manipulating external magnetic field parameters. Under static gradient magnetic fields, viscous response dominates and the robot deforms like a liquid; under rotating magnetic fields, the robot shows elastic deformation and rigid-body movements. (**B**) The antibiofilm robot is capable of crossing over undulating surfaces under rotating magnetic fields and deforming to remove biofilms in deep crevices under gradient magnetic fields. The adaptability is highly desired for eradicating biofilm infections on complex surface topographies such as medical meshes and metallic stents. (**C**) The antibiofilm robot functions by mechanically destroying the biofilm matrix while releasing antimicrobial agents to kill bacterial cells. Meanwhile, disrupted biofilm debris is collected by the robot through covalent bonding and removed to prevent biofilm regrowth. (**D**) The imaging-guided antibiofilm treatment has several building blocks: First, deliver the antibiofilm robot through endoscopy; then, track the robot with endoscope imaging or x-ray fluoroscopy; with the visual feedback, an operator can control the movement of the antibiofilm robot by moving the robotic arm–magnet system via a joystick. The tracking and navigation are demonstrated in an ex vivo porcine bile duct. (B) used pictures from Servier Medical Art as material under the Creative Common Attribution 4.0 license: http://creativecommons.org/licenses/by/4.0/.

from sinking (movie S1). Taking advantage of such a rate-dependent behavior, we can use different magnetic fields to drive the robot to better adapt to the environment. For instance, in a biofilm eradication task in the human body, rotating magnetic fields are used to drive the robot across undulating surfaces to reach the target location, and static gradient magnetic fields are used to induce large deformation of the robot to reach deep crevices to remove biofilms within. Figure S4 shows that the robot deforms and navigates through narrow canyons and S-shaped tunnels under a static gradient magnetic field and crosses over undulating surfaces under a rotating magnetic field. Robots with different sizes from 0.5 to 20 mm can be well navigated to travel a curved tube (fig. S5), while movements of robots smaller than 0.5 mm may be limited by low driving force, surface adhesion, and fast disintegration. A magnetic gradient field of ~8.2 T/m does not change the spatial distribution of magnetic particles in the hydrogel matrix (fig. S6).

We define three representative locomotion modes of the antibiofilm robot, namely, the T-mode (translational movement), R-mode (rotational movement), and TR-mode (combination of translation and rotation, Fig. 2D). We implement a robotic actuation system for generating the magnetic fields for driving different locomotion modes of the robot: A permanent magnet is mounted on the robotic arm, and its rotational and translational movement can be individually controlled via a joystick or computer scripts. In the T-mode of motion, the robot is put on a substrate and the magnet is placed under the substrate with only translational movement actuated. Consequently,

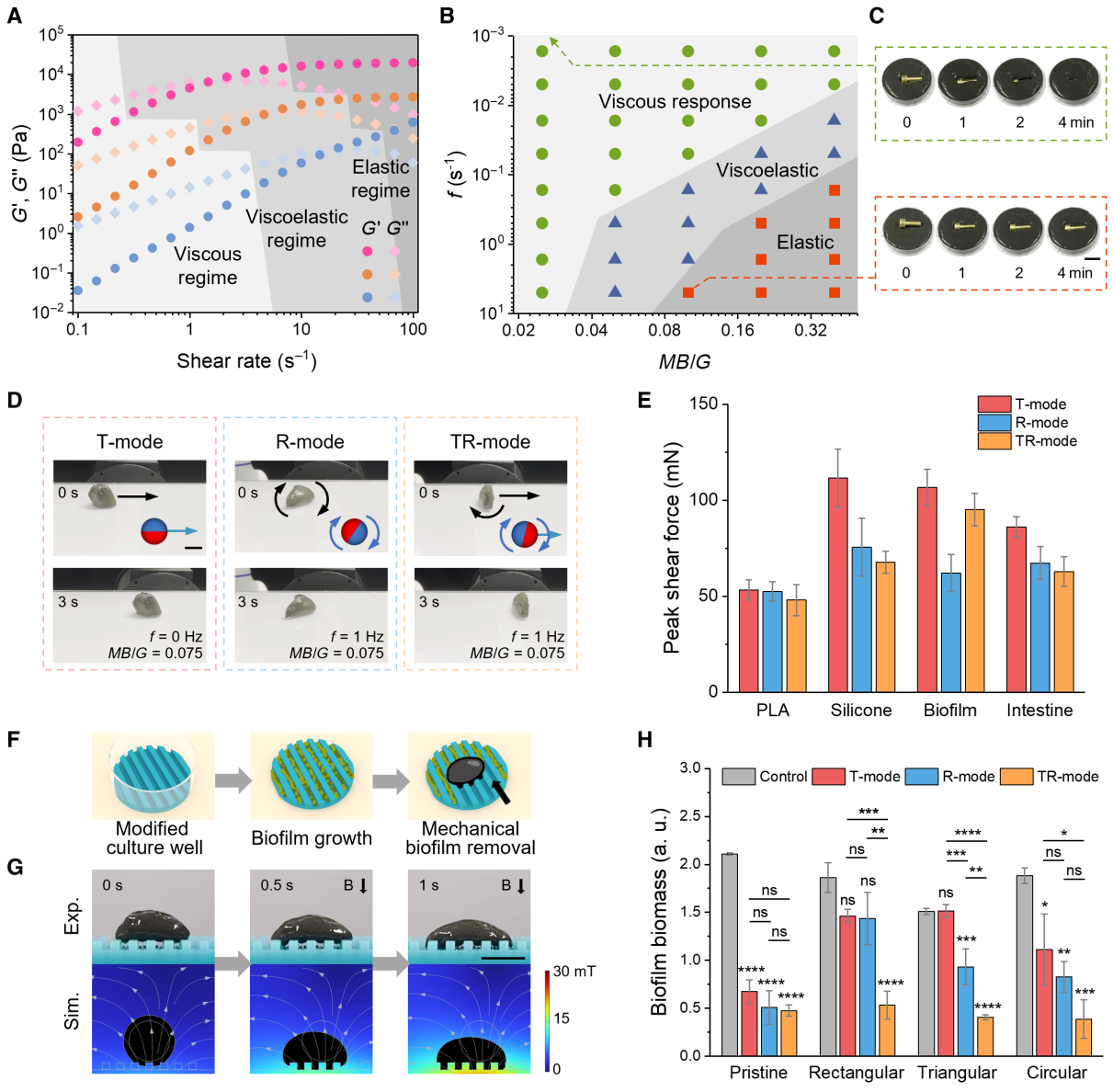

Fig. 2. Characterization, locomotion, and mechanical biofilm removal. (**A**) The storage modulus (G') and loss modulus (G'') of the antibiofilm robots with different cross-linking ratio C (the mass ratio between monomer and cross-linker). The robots demonstrate viscous liquid–like response under low shear rates and elastic response under high shear rates. Pink: $C = 0.05$; brown: $C = 0.025$; blue: $C = 0.0167$. (**B**) Phase diagram of the antibiofilm robot's viscoelastic response under rotating magnetic fields. The viscoelastic response of the robot can be triggered by external magnetic fields. (**C**) Without applying a rotating magnetic field, a brass screw sinks into the viscous magnetic hydrogel, while under a rotating magnetic field, the hydrogel hardens and supports the screw from sinking. (**D**) Three distinct locomotion modes under different actuations: T-mode corresponds to translational movements under static gradient magnetic fields, R-mode corresponds to rotational movements under rotational magnetic fields, and TR-mode corresponds to combined movements under gradient rotating magnetic fields. (**E**) Peak shear force induced by the three locomotion modes of the antibiofilm robot (1 g with 20 wt % NdFeB) on different substrates. (**F**) Schematic of the mechanical biofilm removal test on modified culture wells with different surface topographies. (**G**) Experiment and simulation results under an increased gradient magnetic field from approximately 22 to 45 mT; the antibiofilm robot deforms and reaches the bottom of the rectangular substrate. (**H**) Remaining biofilm biomass on the modified culture wells with different topographies after mechanical biofilm removal. ns, not significant; $^*P < 0.05$; $^{**}P < 0.01$; $^{***}P < 0.001$; $^{****}P < 0.0001$ by one-way analysis of variance with Tukey's multiple comparisons test. Scale bars, 10 mm.

the antibiofilm robot experiences magnetic body force and moves across the substrate with a magnetic flux density of $|\mathbf{B}| = 28.4$ mT, a magnetic field gradient $|\nabla \mathbf{B}| = 1039.8$ mT/m, and a translational speed of the robot arm, $v = 2$ mm/s. However, the movement becomes impossible when the magnet ball is placed farther away ($|\mathbf{B}| = 10.7$ mT, $|\nabla \mathbf{B}| = 261.0$ mT/m), or when the robot arm moves rapidly ($v = 20$ mm/s). Upon turning off the translational movement of the robot arm and activating the rotation of the magnet ball, the antibiofilm robot's motion is mainly driven by magnetic torque, resulting in a cyclic rolling motion on the substrate. It is noteworthy that rotating magnetic fields also facilitate the rearrangement of magnetic particle chains inside the robot, therefore maintaining homogeneous distribution and avoiding leakage of magnetic particles. Such a phenomenon has been discovered on magnetic nanoparticle

swarms and magnetic droplet collectives (*10*, *52*–*54*). However, the R-mode has a limited motion range and cannot propel the robot to navigate inside the body. To navigate across complex terrains, a TR-mode combining translational and rotational movement is necessary. While the T-mode fails to maneuver the robot across the obstacles, the TR-mode successfully enables the robot to traverse obstacles (movie S2).

Large force output is essential for mechanically removing biofilms and can be achieved by applying strong magnetic fields. However, it is often impossible in clinical situations to place the magnet close to the biofilm site due to obstruction of the human body. For microrobotic surgeries, magnetic torque–driven movement is more favorable than magnetic body force–driven movement, because magnetic torques and forces are proportional to r^{-3} and r^{-4}, respectively (r is the distance between the center of the robot and the magnet) (*55*). We estimate the maximum force and torque output by 1 g of the antibiofilm robot to be $F = 95.45$ mN and $\tau = 1.25$ mN · m at $r = 50$ mm, a typical condition for in vitro and small animal experiments (fig. S7). However, the force and torque output drop drastically to $F = 1.05$ mN and $\tau = 0.057$ mN · m at $r = 150$ mm, corresponding to a distance for deep-buried body regions such as the gastrointestinal tract (tables S2 to S4 and text S3). Next, we experimentally quantify the shear force exerted on the substrate by the antibiofilm robot. On a porcine small intestine surface, the peak shearing force is 86.15 ± 5.34 mN (mean ± SD) for the T-mode, 67.31 ± 8.53 mN for the R-mode, and 62.87 ± 7.78 mN for the TR-mode. In addition, we also measure the shearing force on different substrates, including three-dimensional (3D)–printed polylactic acid (PLA), silicone elastomer, and *Escherichia coli* biofilm colonized surface (Fig. 2E). For all substrates tested, the T-mode yields the highest shearing force on the substrate at the same distance D between the magnet and the substrate, while the TR-mode achieves 60 to 90% of the T-mode's force (fig. S8). On the basis of such measurements, we estimate that the shear stress exerted on the *E. coli* biofilm colonized surface is 1.21 ± 0.11 kPa under the TR-mode. On the other hand, the creep compliance of 2-day *E. coli* biofilm lies on the magnitude of 1 to 10 Pa^{-1} measured by a particle-tracking microrheology (fig. S9). However, there is no solid basis to predict whether such a stress level is sufficient to destroy the biofilm due to the lack of biofilm mechanical models. The reported biofilm mechanical strength ranges from a few pascals to 19,000 Pa depending on test methods, culture environments, bacteria strains, etc. (*56*, *57*). To determine the efficacy of mechanical biofilm removal, we culture *E. coli* biofilm on pristine and modified culture wells with rectangular, triangular, and circular topographies. Subsequently, we activate the antibiofilm robot to mechanically remove the biofilm from these surfaces (Fig. 2F and movie S3). Without applying a magnetic field, the robot maintains its shape for a certain period of time and does not fill in the trenches across all three topographies. However, upon applying a magnetic field of approximately 45.2 mT, the robot undergoes large deformation and reaches the bottom of the trenches in a short time (fig. S10). The liquid-like deformation behavior is also reproduced by a finite element simulation using a phase-field model (Fig. 2G). Such shape adaptability is beneficial for removing biofilms in hard-to-reach regions. In the pristine culture wells with flat surfaces, all three modes of locomotion reduce biofilm biomass significantly (Fig. 2H). However, the effectiveness of the mechanical treatment declines sharply for modified culture wells, with persistent bacterial colonization unremoved at the bottom of trenches (fig. S11). Nevertheless, experimental results suggest a positive correlation between biofilm removal rate and applied magnetic field strength, and the TR-mode has the highest efficiency among the three modes in mechanically removing biofilm on complex surface topographies.

In vitro antibiofilm performance

Even though biofilms are mechanically removed from an implant surface, biofilm debris can still cause negative impacts, such as biofilm regrowth at other sites or even fatal septicemia (*25*). To prevent the dispersal of living biofilm fragments, the most commonly used strategy is to deactivate bacterial cells within the biofilm during mechanical disruption. Reported examples include antibiofilm robots releasing reactive oxygen (*30*–*36*, *40*)/nitrogen (*58*, *59*) species, antibiotics (*39*, *60*), and antimicrobial peptides (*38*). Another potential strategy, to capture and remove biofilm debris, remains unexplored. Here, we use the dynamic covalent bonding between the antibiofilm robot and the biofilm matrix to collect biofilm debris. As illustrated in Fig. 3A, Gram-negative *E. coli* or Gram-positive methicillin-resistant *Staphylococcus aureus* (MRSA) biofilms are cultured on the bottom surface of culture dishes and treated by the antibiofilm robot. Actuated by a rotating magnetic field, the robot exhibits rotational motion on the bottom surface of the petri dish, mechanically destroying the biofilm matrix and capturing biofilm debris simultaneously. The adhesive interaction between the antibiofilm robot and the biofilm matrix is explained as the covalent bonding effect between boronic esters and diols of carbohydrates, which are the major components of EPS (as illustrated in Fig. 3B) (*61*). After the treatment, the biofilm's dry weight is significantly reduced without rinsing, indicating efficient biomass removal by the antibiofilm robot in both liquid and air environments (Fig. 3C and fig. S12). Subsequent staining using the crystal violet method reveals a clear area at the dish's center where the antibiofilm robot was deployed (Fig. 3D).

However, mechanical treatment and collection of biofilm debris do not lead to eradication. To effectively eliminate the planktonic bacteria cells, two different antimicrobial agents are loaded with the antibiofilm robot, and their antibiofilm performance is evaluated. Levofloxacin, a common broad-spectrum antibiotic, exhibits a characteristic peak at 288 nm under an ultraviolet (UV)–visible light spectrometer, making it suitable as a model drug for investigating the drug release kinetics of the antibiofilm robot. We first assess the stability of the antibiofilm robot in a liquid environment. It is found that the antibiofilm robot with high cross-linking density ($C = 0.05$) retains more than 80% of the initial mass after 60 min of immersion and that with low cross-linking density ($C = 0.0167$) degraded completely within 30 min. Under rotating magnetic fields, the antibiofilm robot degrades much faster (fig. S13A); such a feature could be used to accelerate drug release (*62*). The degradation rate also increases in acid physiological conditions such as intestinal and gastric fluids because boronic ester bonds favor disassociation at acid pH (fig. S13, B and C) (*47*). To determine the drug release kinetics under rotating and static magnetic fields, we fabricate antibiofilm robots with different initial loading concentrations of levofloxacin, place them into a petri dish, and apply the magnetic field. The absorbance of the solution at 288 nm gradually increases with time due to the released levofloxacin from the antibiofilm robot (fig. S14A). At low concentrations, the relationship between levofloxacin concentration and absorbance at 288 nm of the solution is linear (fig. S14, B and C). Using a linear fitting, we plot the relationship between cumulative drug release concentration and immersion time of the antibiofilm robot in fig. S14D. The

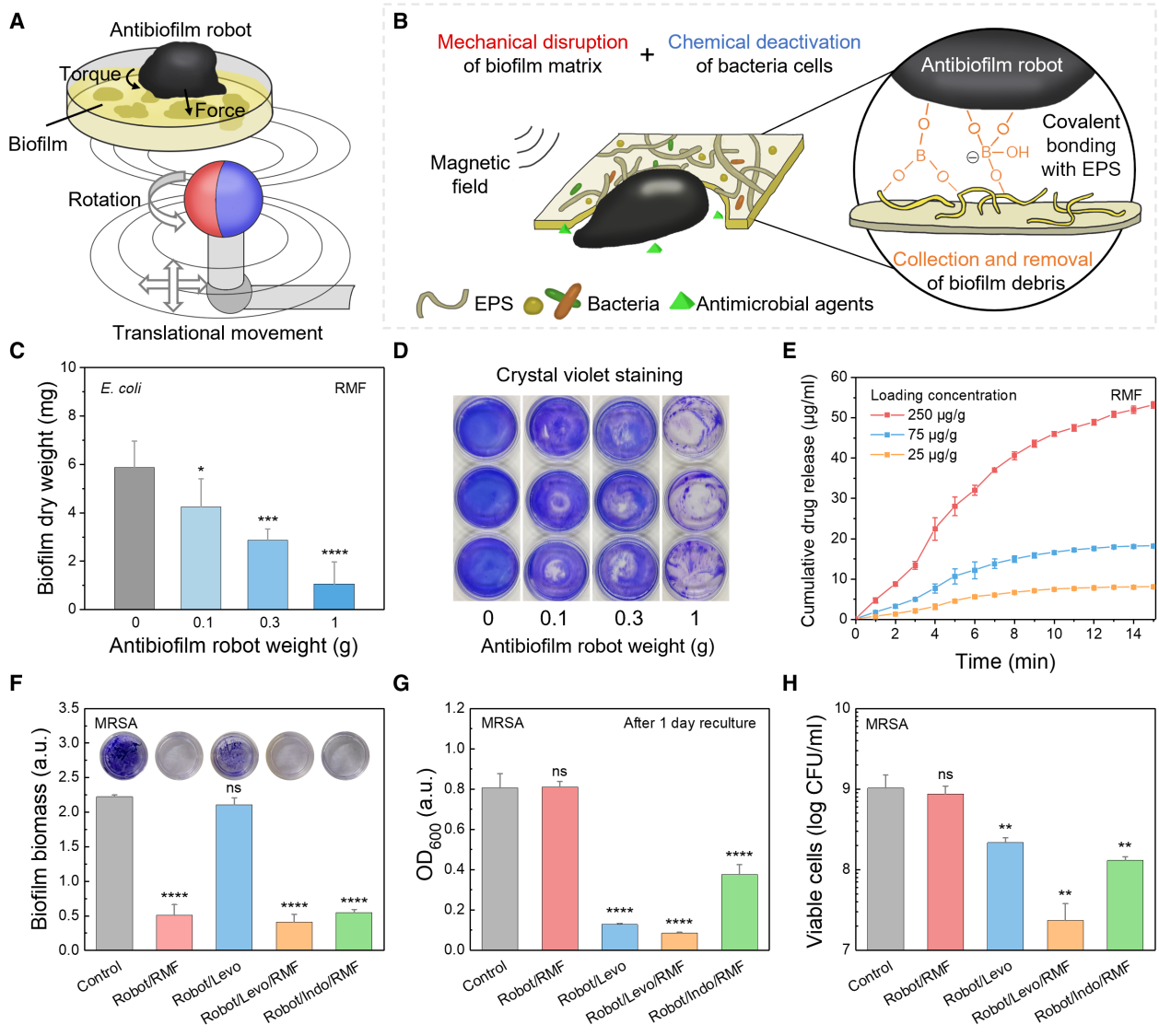

Fig. 3. In vitro antibiofilm performance. (**A**) Schematic of the experimental setup. Under a typical experimental condition, the magnetic flux density norm applied on the antibiofilm robot is approximately 24 mT. As a result, the robot is subject to magnetic force and torque to move on the substrate. (**B**) Schematic of the covalent bonding between the antibiofilm robot and the biofilm extracellular polymeric substances (EPS), which enabled adhesion and collection of biofilm debris by the antibiofilm robot. (**C**) Biofilm dry weight measurement and (**D**) stained biofilm on a 35-mm petri dish after being treated by the antibiofilm robot. (**E**) Characterization of levofloxacin release by the antibiofilm robot through absorbance at 288 nm. (**F**) The biofilm biomass assessment, (**G**) the optical density of the bacterial solution, and (**H**) the viable cells count after different treatments. RMF, rotating magnetic field. Robot/RMF: The antibiofilm robot was magnetically actuated to perform mechanical biofilm removal; Robot/Levo: The antibiofilm robot was loaded with levofloxacin and immersed into the bacterial broth, but no magnetic field was applied; Robot/Levo/RMF: The antibiofilm robot loaded with levofloxacin was magnetically actuated to remove biofilm and release the carried drug; Robot/Indo/RMF: The antibiofilm robot loaded with indolicidin was magnetically actuated to remove biofilm and release the carried drug. *$P < 0.05$; **$P < 0.01$; ***$P < 0.001$; ****$P < 0.0001$ by one-way analysis of variance with Dunnett's multiple comparisons test.

released levofloxacin concentrations in solution are 14.39, 4.04, and 1.56 μg/ml at 5 min for initial loading concentrations of 250, 75, and 25 μg/g, respectively. The released concentrations then gradually increase to 33.24, 11.14, and 5.27 μg/ml at 60 min. The release rates are much higher with a rotating magnetic field (Fig. 3E). After only 5 min, the released levofloxacin concentrations are 28.02, 10.64, and 4.55 μg/ml for three different initial loading concentrations, approaching the concentrations achieved after 35 min of static immersion. Among the antibiofilm robot's three locomotion modes, the TR-mode shows the fastest drug release (fig. S14E).

To investigate the antibiofilm efficacy of the proposed robot, different treatments are applied to the MRSA biofilm, namely, Robot/RMF, where the antibiofilm robot is applied and actuated to mechanically remove biofilm (movie S4), but no antimicrobial is carried by the robot; Robot/Levo, where the antibiofilm robot loaded with levofloxacin (250 μg/g) is applied to the well, but no magnetic field is applied; Robot/Levo/RMF, where the antibiofilm robot loaded with levofloxacin (250 μg/g) is applied and actuated by a rotating magnetic field to remove biofilm and release the carried antimicrobial content; and Robot/Indo/RMF, where the antibiofilm robot loaded

with indolicidin (0.25 μg/g) is applied and actuated. After the treatments, a crystal violet staining assay is performed to assess the biofilm biomass in the wells. Results suggest that the biofilm biomass of the Robot/RMF-, the Robot/Levo/RMF-, and the Robot/Indo/RMF-treated groups is significantly reduced compared to the control group by 77.10, 81.64, and 75.38%, respectively (Fig. 3F). However, the Robot/Levo-treated group shows no significant difference compared to the control. This underscores the importance of magnetic actuation of the antibiofilm robot in mechanically disrupting and removing biofilm from the substrate. Subsequently, bacteria reculture, live/dead staining, and plate counting are performed to assess the viability of bacteria cells after treatment. After 1 day of reculture, the optical density of the bacterial solution of the Robot/Levo-, Robot/Levo/RMF-, and Robot/Indo/RMF-treated groups is significantly lower than the control (15.81, 10.45, and 46.70% of the control, respectively, Fig. 3G). However, the Robot/RMF group with no antimicrobial content released has a comparable optical density (100.61%) to the control, suggesting that mechanical disruption of the biofilm matrix alone does not kill or deactivate bacteria cells. The results from live/dead assay (fig. S15) and plate counting (Fig. 3H) confirm the synergistic antibiofilm effect, where the Robot/Levo/RMF-treated group demonstrates the largest decrease in the count of viable cells (97.73%) compared to the Robot/RMF-treated (15.24%) or the Robot/Levo-treated (78.93%) group. The Robot/Indo/RMF group, however, exhibits a good bactericidal effect (87.36%) with only 1/1000 drug loading concentration compared to the levofloxacin-loaded robot [indolicidin (0.25 μg/g) versus levofloxacin (250 μg/g)]. Such a result highlights the potential application of leveraging microrobotic delivery of antimicrobial agents such as antimicrobial peptides to treat biofilm infection without causing antimicrobial resistance. The antibiofilm robot loaded with antimicrobials also exhibits a powerful ability against *E. coli* biofilm (fig. S16).

Biofilm removal on the mesh and stent

We evaluate the antibiofilm robot's performance on biological surfaces with complex topographies such as a hernia mesh and a metallic biliary stent. A hernia mesh serves as a scaffold supporting tissues around hernias, a condition commonly occurring in the abdominal region. Infection of implanted hernia mesh is a severe complication that often requires a second surgery to remove the infected mesh, where the most common bacterial species found is MRSA (*63*). To prevent postoperation infection, systemic administration of antibiotics is commonly practiced. Besides, hernia meshes with antibacterial coating have been used to delay bacterial adherence to the mesh surface (*64*). Still, current technology cannot guarantee the prevention of bacteria colonization. Here, we test the efficacy of the liquid-bodied antibiofilm robot in eliminating the established MRSA biofilm on a hernia mesh. The mesh is cocultured with bacterial broth to allow biofilm formation and then sutured onto the surface of a porcine small intestine ex vivo (Fig. 4A). The scanning electron microscopy (SEM) images confirm the intensive colonization of the MRSA biofilm on the mesh (Fig. 4B). It also shows the complex topologically entangled structure in the 3D fabric network, which causes great challenges to clear biofilm colonization within. The antibiofilm robot is applied onto the hernia mesh and actuated to remove the biofilm and at the same time release the antimicrobial content (movie S5). After treatment, a crystal violet assay and a plate count are performed to evaluate the antibiofilm efficacy. The biofilm biomass is reduced by 84.25% after the treatment, suggesting that the antibiofilm robot removed most biofilms colonized on the mesh. Then, living bacteria are detached from the mesh and counted. The bacteria count is approximately 3×10^3 colony-forming units (CFU) per sample from the control. In contrast, no living colony is found in the antibiofilm robot–treated sample, suggesting the deactivation of bacteria cells after the treatment.

Next, we test the antibiofilm robot on a metallic biliary stent (Fig. 4E). Biofilm formation within the bile duct substantially contributes to the development of biliary sludge, pigment gallstones, and biliary stent obstruction (*65*). Plastic and metallic stents are commonly used for endoscopic biliary drainage. Compared with plastic stents, metallic biliary stents fabricated by shape-memory alloy (nitinol) have a self-expansion force to support the bile duct, thereby creating a larger lumen caliber. However, the metal wires also result in uneven terrain and crevices in the lumen, causing difficulties for the miniature robots' movement. The stent with biofilm colonization is installed into a silicone tube to mimic the bile duct. The antibiofilm robot is deployed from one opening of the stent and actuated by a rotating gradient magnetic field to navigate back and forth (Fig. 4F and movie S6). After 5 min of treatment, the viability of the biofilm on the stent is examined by a live/dead staining assay and a plate count method. The live/dead staining images reveal that 87.37% of bacteria are dead after treatment (Fig. 4G), and the plate count suggests an 81.82% reduction in living cells (Fig. 4H).

In vivo antibiofilm experiments

A robotic surgery platform is proposed for in vivo imaging-guided navigation and actuation of the liquid-bodied antibiofilm robot (Fig. 5A). The platform consists of a robotic actuation system (consisting of the Φ50-mm magnet setup), an endoscope for direct visual imaging, and an x-ray machine for imaging in deep regions (fig. S17). An uncovered biliary stent is installed in the ex vivo porcine bile duct, and the endoscope and x-ray machine are used to track the locomotion of the antibiofilm robot. After deployment with a catheter, the antibiofilm robot is actuated by a rotating gradient magnetic field to navigate through the porcine bile duct (movie S7). The endoscopic view clearly shows the bile duct supported by the stent (Fig. 5B). The inner surface of the bile duct features mesh-like metal wires, creating a challenging topography for microparticle-based or microrod-based antibiofilm robots. In addition, the wet surfaces with viscous biofluids and liquid-gas interfaces are difficult to overcome for microparticle-based robots. In contrast, the liquid-bodied antibiofilm robot demonstrates remarkable adaptivity in navigating through the bile duct under magnetic actuation (Fig. 5B and movie S7).

To assess the performance of the antibiofilm robot in vivo, we develop a mouse model with biofilm infection on indwelled implants. Mice are divided into two groups, namely, control and treatment. Both groups receive implantation of infected stents, but only the treatment group undergoes antibiofilm robot treatment. First, segmented metallic stents are cocultured with bacterial broth for 3 days to form biofilm colonization on the surface. The SEM figures show the bacterial colonization on the stents (fig. S18). Then, the stents are indwelled into the mice's abdominal cavity by surgery. After 4 days, the infected stents are treated with the antibiofilm robot to remove the biofilm and kill the bacteria cells (Fig. 5C). As shown in Fig. 5D and movie S8, the antibiofilm robot is delivered through an incision on the mice's lower abdomen and actuated to remove biofilm and release the carried antimicrobial agent levofloxacin.

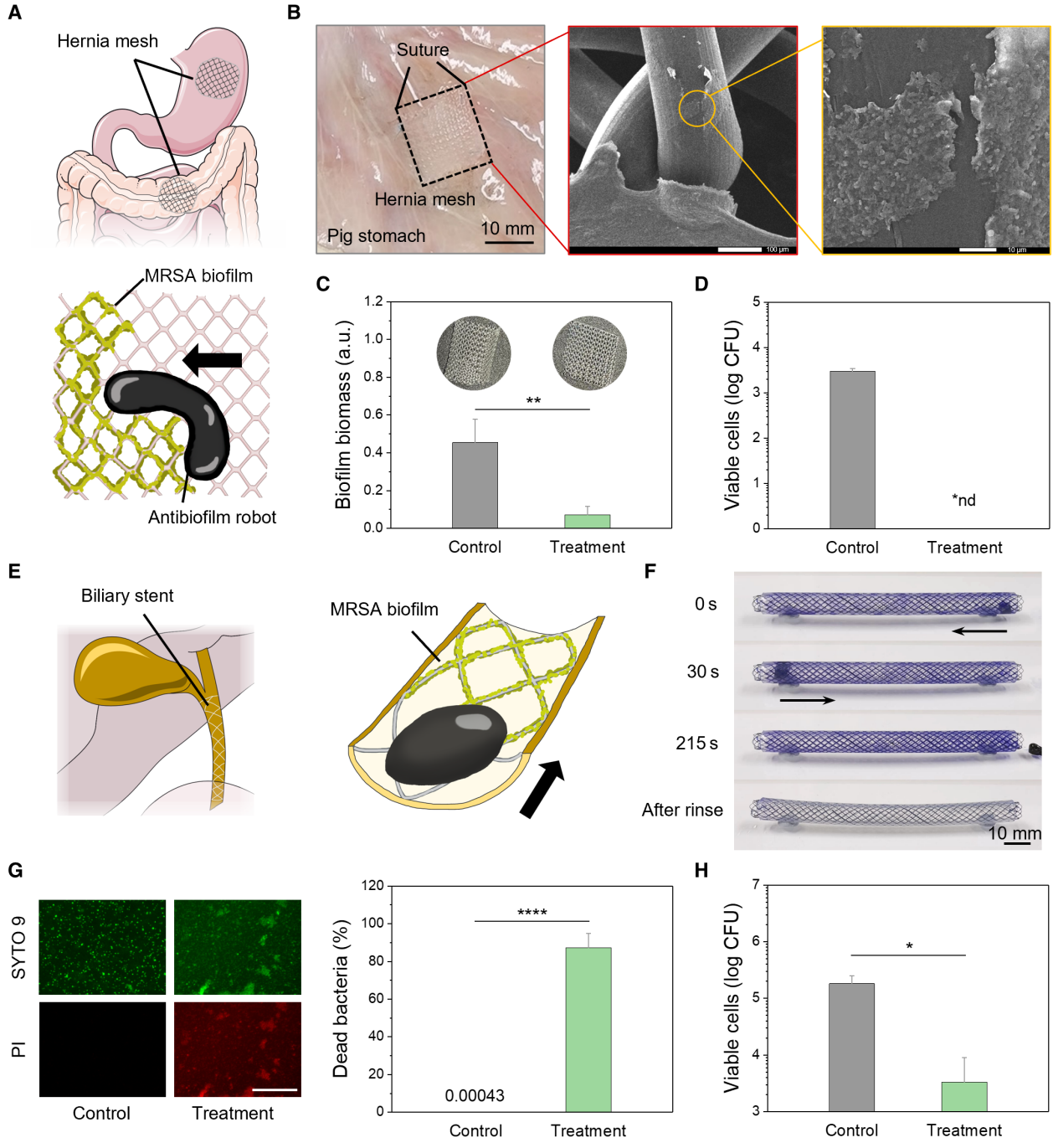

Fig. 4. Biofilm removal on various biological surfaces. (**A**) Schematic depicting the biofilm infection on a hernia mesh. (**B**) Photo of a piece of hernia mesh sutured onto porcine stomach ex vivo, and the zoomed-in scanning electron microscopic (SEM) images of the colonized MRSA biofilm. (**C**) Biofilm biomass on the hernia mesh after the antibiofilm treatment. (**D**) Bacteria count on the hernia mesh after the antibiofilm treatment. nd, not detectable. (**E**) Schematic of biofilm infection on a biliary stent. (**F**) Snapshots of the antibiofilm robot navigating through the biliary stent to remove biofilm. The biofilm is already stained with crystal violet. (**G**) Live/dead staining of biofilm collected from the biliary stent. PI, propidium iodide. Scale bar, 500 μm. (**H**) Bacteria count on the biliary stent after the antibiofilm treatment. *$P < 0.05$; **$P < 0.01$; ****$P < 0.0001$. [(A) and (E)] used pictures from Servier Medical Art as material under the Creative Common Attribution 4.0 license: http://creativecommons.org/licenses/by/4.0/.

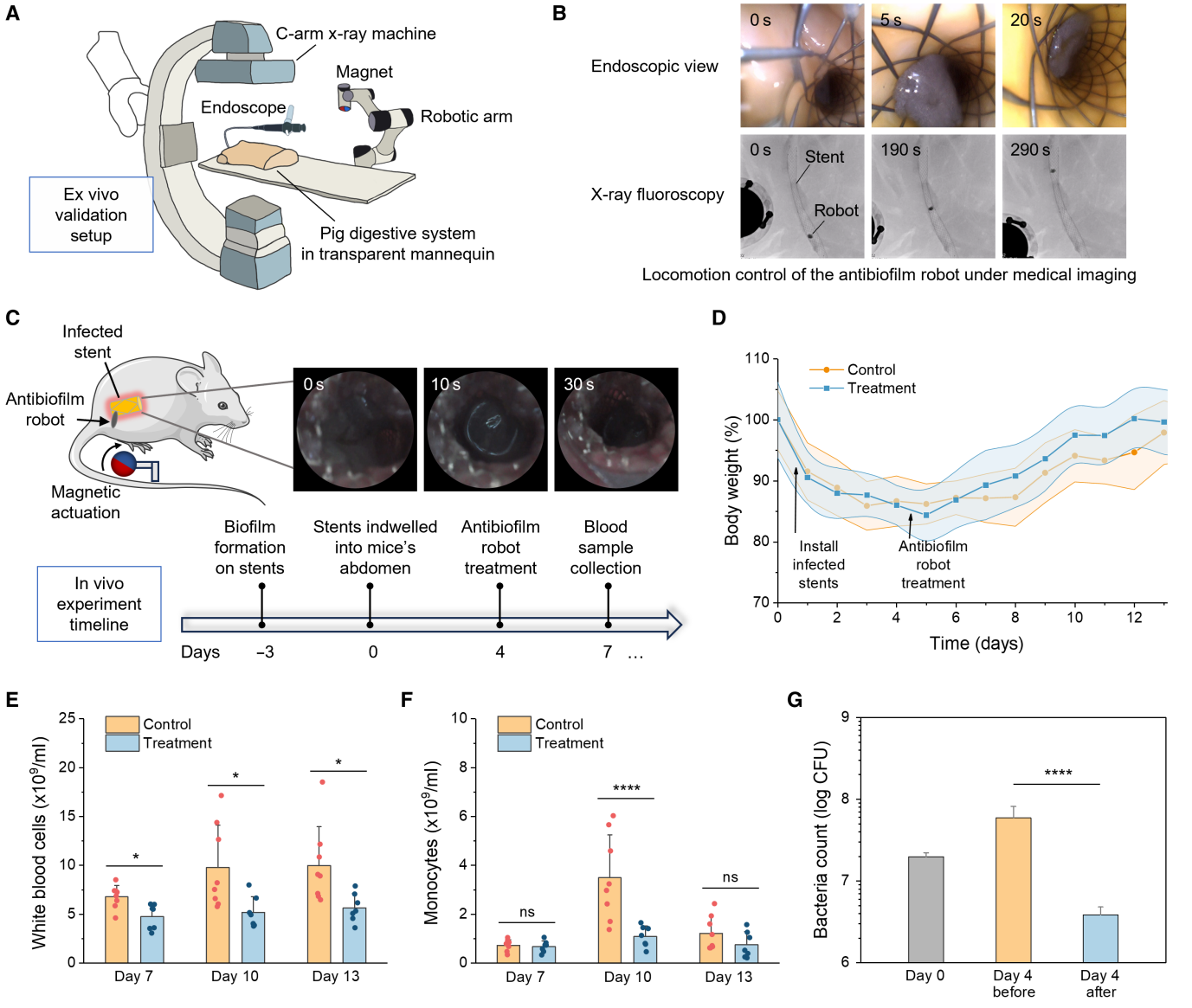

Fig. 5. In vivo antibiofilm experiments. (**A**) The robotic surgery platform consists of a magnetic actuation system, a medical endoscope for delivery and retrieval, and a C-arm x-ray for tracking and imaging. (**B**) Ex vivo validation of the antibiofilm robot navigating in the porcine bile duct with implanted human biliary stent. (**C**) Timeline for the in vivo antibiofilm experiment. The fragmented stents are cocultured with bacterial broth for 3 days and then indwelled into mice's abdominal cavity. The antibiofilm robot is deployed into the inner cavity of the infected stent and activated for antibiofilm treatment. (**D**) Body weight of the mice during the experiment period. (**E**) White blood cell count and (**F**) monocyte count in mice blood samples on days 7, 10, and 13. *$P < 0.05$; ****$P < 0.0001$ by two-way analysis of variance with Holm-Šídák's multiple comparisons test. Error bars are the SD of measurements ($n = 7$ for the treatment group and $n = 8$ for the control). (**G**) Bacteria count on the stents (per sample) on day 0 before implantation, and day 4 before and after the antibiofilm treatment. ****$P < 0.0001$. (C) used pictures from Servier Medical Art as material under the Creative Common Attribution 4.0 license: http://creativecommons.org/licenses/by/4.0/.

Both groups show notable body weight loss on day 1 (Fig. 5E) due to the major surgery for stent installation. However, after the antibiofilm robot treatment on day 4, mice in the treatment group show a faster recovery of body weight compared to the control group. By day 12, the average body weight for the treatment group has recovered to 100.20 ± 4.86% of the initial weight, while for the control group, the number is only 94.67 ± 6.11%. To further study the efficacy of the antibiofilm robot treatment, blood samples from the mice are analyzed. White blood cell count provides valuable information about microbial infection inside the body. An increase in white blood cell count after installation of the infected stent is observed for both experimental groups. However, mice from the treatment group show lower white blood cell count than the control on day 7 (4.76 ± 1.30 versus 6.79 ± 1.18 × 10^9/ml), day 10 (5.20 ± 1.59 versus 9.79 ± 4.43 × 10^9/ml), and day 13 (5.67 ± 1.47 versus 9.99 ± 3.98 × 10^9/ml), suggesting a lower level of inflammation (Fig. 5F). Monocytes are white blood cells that can differentiate into macrophages, which are essential for combating chronic infections. The monocyte counts for both groups peak on day 10, with 3.50 ± 1.64 × 10^9/ml for the control and 1.10 ± 0.40 × 10^9/ml for the

treatment group (Fig. 5G). Last, the bacteria count on the indwelled stents is examined before and after the antibiofilm treatment. The bacterial colony-forming unit derived from the stent exhibits a reduction of 93.45% subsequent to the treatment, thereby suggesting a noteworthy bactericidal efficacy of the antibiofilm robot (Fig. 5H). In summary, mice in the experiment underwent a loss in body weight and a rise in white blood cell count due to the inflammatory response following the installation of the infected stents. However, the treatment group demonstrates better recovery of body weight and lower levels of inflammation after the treatment, indicating effective biofilm removal and antibacterial effects of the antibiofilm robot.

DISCUSSION

We developed a liquid-bodied antibiofilm robot for effectively eliminating biofilm infections on medical meshes and stents. We found that the viscoelastic response of the robot is governed by two distinct timescales: the actuation time corresponding to applied magnetic field parameters and the intrinsic relaxation time of the material. This switchable viscoelastic response is vital for maneuvering within body cavities and eliminating biofilms on intricate topographies such as medical stents and meshes. The proposed robot integrates various antibiofilm mechanisms, including mechanical disruption of the biofilm matrix, chemical deactivation of bacterial cells, and collection of biofilm debris. We evaluated the robot's efficacy in vitro on medical implants such as a hernia mesh and a metallic biliary stent. The robot can be delivered via endoscopy and tracked by x-ray fluoroscopy, and the feasibility of the platform has been demonstrated on ex vivo pig organs. Last, we established an in vivo implant infection model and demonstrated the robot's potent ability to combat biofilm infections in the mouse model.

The current study faces several limitations. First, the biofilm infection model established in mice lacks full clinical representation as it does not allow for in situ biofilm formation on medical implants. This in situ formation is crucial for studying the microenvironment, the immune responses, and evaluating the potential therapeutic efficacy of antibiofilm treatments (*66*). Moving forward, it would be beneficial to use larger animals that naturally develop biofilm infections for a more accurate assessment.

The current robot loads broad-spectrum antibacterial agents as ammunition to kill bacteria. Novel antibacterial agents, such as antibacterial nanoparticles, biofilm-degrading enzymes, and quorum sensing inhibitors, could be coupled with the antibiofilm robot to be delivered into the biofilm site. In addition, species-specific antimicrobials could be combined with the robot to enhance therapeutic outcomes against specific infections.

The dynamic nature of the antibiofilm robot constrains its operational region within the body. Although experiments suggest that the robot will retain most of its weight in 10 to 20 min, which is the time of a microrobotic intervention, detachment of magnetic particles from the robot's surface can be found especially under acidic conditions. The biocompatibility of these particles in different tracts in the human body, though coated with a protective silicon layer, needs further confirmation. Implementing enteric-coated capsules can shield the robot from gastric acid and ensure safe passage to the intestinal region. Alternatively, a recent study suggests using 2-acrylamidophenylboronic acid to construct dynamically cross-linked hydrogels capable of self-healing under acidic pH (*67*). Material innovations may expand the lifetime of the proposed antibiofilm robot and make it applicable to acidic physiological environments.

MATERIALS AND METHODS

Preparation of the antibiofilm robot

Polyvinyl alcohol (PVA, Sigma-Aldrich 363170) was dissolved in deionized water in a mass ratio of 16:84. Meanwhile, sodium tetraborate (Maclin S818104) was dissolved in deionized water in a mass ratio of 1:99. Both solutions were heated at 95°C and stirred overnight to achieve complete dissolution. Levofloxacin (Aladdin 157745) and indolicidin (trifluoroacetic acid removed, NovoPro Bioscience) were dissolved in phosphate-buffered saline (PBS) solution to 10 mg ml^{-1} and 10 μg ml^{-1}, respectively. NdFeB microparticles (average size of 5 μm, Guangzhou Xinnuode Co. Ltd.) were coated with SiO_2 via the Stöber method (*45*). To make the antibiofilm robot, the PVA solution, the borate solution, NdFeB microparticles, and levofloxacin and/or indolicidin were mixed at certain mass ratios. Typically, 1 g of NdFeB microparticles and 1.25 mg of levofloxacin were mixed with 2 g of the PVA solution and stirred thoroughly. The resultant solution was then mixed with 2 g of the borate solution and stirred to obtain a slimy mixture. Last, the mixture was magnetized by a 1.7-T impulse magnetic field. Antibiofilm robots with different concentrations of antimicrobials or cross-linkers were prepared similarly.

Magnetic actuation setup

Two setups were used to drive the antibiofilm robot. The first setup comprises an N52-grade NdFeB ball magnet (diameter, 50 mm), a motor, and a robotic arm. The second setup comprises an N52-grade NdFeB ball magnet (diameter, 25 mm) and a motor. In vitro and ex vivo experiments were done with the Φ50-mm ball magnet setup, while the motion trajectories of the robotic arm were programmed via computer scripts or directly controlled with a joystick, and the rotation of the motor was controlled with a computer script. In vivo experiments were done with the Φ25-mm ball magnet setup. The magnetic fields generated by two setups are simulated and discussed in text S3.

Biofilm culture

Freeze-dried *E. coli* [American Type Culture Collection (ATCC) 25922] or MRSA (ATCC 43300) was cultured with Luria Bertani (LB) broth and brain heart infusion broth, respectively. The bacterial culture was shaken at 170 rpm under 37°C for 2 days and then transferred to a 24-well plate (Nunc 142475, Thermo Fisher Scientific). One hundred microliters of the bacterial culture (~10^8 CFU ml^{-1}) was added to each well along with 1 ml of fresh broth. The 24-well plate was then put into an incubator for another 2 days under 37°C for biofilm formation.

Mechanical and rheological tests

The shear force imposed by the antibiofilm robot on different surfaces was measured by a micromechanical testing system (Biomomentum Mach-1 V500cst) with a 1.5 N loading cell. First, PLA substrates were printed with a commercial extrusion printer. Silicone thin film or porcine intestine segments were glued to the substrate, and the biofilm surface was prepared by culturing *E. coli* on the PLA substrate for 2 days. For testing, the loading cell was installed horizontally, connecting to the substrates. The antibiofilm robot (1 g) was put on the surface and actuated by the magnetic actuation setup under the same condition (D = 45 mm). Blank tests were conducted and extracted

from the experimental curves to eliminate the effect of the magnetic force on the loading cell. To measure the rheological properties of the antibiofilm robots, frequency sweep was performed with a 60-mm parallel plate geometry (Discovery HR 20, TA Instruments). The applied strain was set as 1% and the frequency ranged from 0.1 to 100 Hz.

Biofilm removal on modified culture wells

To build a biofilm model on various surface topographies, a 24-well plate was modified with mold-casted silicone elastomer. Briefly, negative molds were first 3D printed with PLA material. Then, a silicone precursor (Ecoflex 00-30) was poured into the wells, the negative molds were applied, and the plate was degassed to remove the bubble in the precursor. After curing under room temperature overnight, negative molds were removed and the bacterial culture (*E. coli* 100 μl × ~10^8 CFU ml^{-1} with 1 ml of fresh broth) was added to each well. The plate was then put into an incubator for 2 days under 37°C for biofilm formation.

To remove the biofilm from the 24-well plate, 1 g of the antibiofilm robot was added into each well, and different magnetic fields (corresponding to the three modes of locomotion) were applied for 5 min. For the T-mode motion, the robotic arm moved at a speed of 10 mm s^{-1}; for the R-mode motion, the rotation frequency was 2 Hz; for the TR-mode, the robotic arm and the motor were activated simultaneously with the above parameters. After the treatment, antibiofilm robots were removed with a magnet, and a crystal violet assay was conducted to access the total biofilm biomass left in each well. The liquid content was gently removed from the wells followed by adding 200 μl of methanol into each well. After 15 min, the liquid was removed, and the wells were washed with PBS. Then, 200 μl of crystal violet solution (1% w/v) was added to each well. Five minutes later, the solution was removed and the wells were washed three times with PBS. Last, 200 μl of acetic acid solution (33% v/v) was added into each well for 30 min to dissolve the stain, and the absorbance of the resultant solution was measured with a UV-visible light spectrophotometer (HITACHI U-2910).

Drug release tests

Drug release tests were carried out in 35-mm petri dishes. Deionized water (4 ml) and 1 g of the antibiofilm robot were added to a petri dish, and the robot was actuated with the magnetic actuation setup at a distance of 30 mm. The robot was taken from the petri dish and weighed at given time intervals. To calculate the drug release rate, the absorbance of levofloxacin solution (5, 10, 15, 20, and 25 μg ml^{-1}) at 288 nm was first measured, and a linear fitting between measured absorbance and levofloxacin concentration was made with $k = 0.066 \pm 0.002$. The robot (1 g) loaded with levofloxacin was put into a petri dish (4 ml of deionized water) and actuated. At the given time intervals, 800 μl of the solution was taken out with a pipette from the edge of the dish, the absorbance of the solution was measured, and the solution was returned to the petri dish. The cumulative drug release concentration was calculated as $c\ [\mu g\ ml^{-1}] = \text{absorbance} / k$.

In vitro antibiofilm performance on well plates

Antibiofilm performance was evaluated by adding 1 g of the antibiofilm robot into each well with biofilm colonization and actuating with the TR-mode for 5 min. After treatment, antibiofilm robots were removed with a magnet and a crystal violet assay was used to access the biofilm biomass as previously described. Meanwhile, 10 μl of bacterial solution from each well was extracted with a pipette and added to 90 μl of fresh broth. After culturing for 24 hours under 37°C, the optical density at 600 nm (OD_{600}) of the culture was measured. In addition, the number of viable cells after treatment was determined by a plate counting method and a live/dead staining assay. For the live/dead staining, a biofilm viability kit (SYTO 9/propidium iodide, Invitrogen L10316) was used with concentrations of 3 and 6 μl ml^{-1} for SYTO 9 and propidium iodide, respectively. After staining for 30 min, fluorescence microscopy was performed. The percentage of live bacteria was calculated as $P_{live} = 1 - (\text{red pixels}/\text{green pixels})$.

Biofilm debris removal

After 2 days of shaking at 37°C, 200 μl of the *E. coli* culture (~10^8 CFU ml^{-1}) was added into a 35-mm petri dish (Nunc 150318, Thermo Fisher Scientific) along with 3 ml of fresh LB broth. The petri dish was then stored at 37°C for 3 days to form a dense biofilm. Then, all liquid suspension was removed and a certain amount of the antibiofilm robot without antimicrobial loading was put into the dish. A rotating magnetic field of 1 Hz and 24 mT or a static magnetic field of 24 mT was applied for 3 min. After that, the antibiofilm robot was retrieved using a small permanent magnet. Last, the petri dish was placed in a fume hood to dry. Biofilm dry weight was calculated as the difference between the final weight of the dish and the initial weight. Crystal violet staining was conducted as previously described.

In vitro antibiofilm performance on mesh and stent

To allow biofilm colonization, hernia mesh (Bard Mesh Pre-Shaped 0113700) and biliary stent (noncovered, Micro-Tech Endoscopy ST03-001-10.100) were put in MRSA culture that had previously been shaken for 2 days and reached a density of ~10^8 CFU ml^{-1} and cocultured for another 3 days. Then, the hernia mesh was cut into small pieces of 1 cm by 1 cm and sutured onto a segment of porcine small intestine bought from the local market. The biliary stent was put into a silicone tube with an inner diameter of 5 mm. For the antibiofilm treatment, antibiofilm robot was deployed and actuated for 5 min with the magnetic actuation setup. Crystal violet assay was performed to determine the biofilm biomass on the hernia mesh. After treatment, the hernia mesh and the biliary stent were transferred to a centrifuge tube containing PBS solution and sonicated for 10 min to detach the bacteria. Last, the number of viable cells in the solution was determined by live/dead staining and the plate count method as previously described. The SEM sample of MRSA-colonized hernia mesh was prepared by immersing the mesh in a 2.5% glutaraldehyde solution for 30 min followed by a gradient dehydration in 30, 50, 70, 90, and 100% ethanol (10 min for each concentration). SEM images were obtained using a JEOL JSM-7800F microscope with a 10-kV accelerating voltage.

Ex vivo navigation in porcine bile duct

Fresh porcine digestive system, including the liver, stomach, gallbladder, and intestine, was purchased from a local market. A biliary stent was installed into the bile duct through a catheter, and the antibiofilm robot (0.5 g) was delivered and actuated by the magnet–robotic arm system and tracked by a medical endoscope and/or a C-arm x-ray machine. The applied magnetic field strength on the robot is estimated to be 3.1 to 28.4 mT.

In vivo antibiofilm experiment

Animal experiment protocols were approved by the Hong Kong Government Department of Health and the Animal Experimentation Ethics Committee of The Chinese University of Hong Kong (Ref. No.

AUP-24-111). Before the experiment, nitinol stent segments with silicone cover (15 mm long and 6 mm in diameter) were immersed in MRSA culture for 3 days at 37°C while shaking at 170 rpm to allow bacteria colonization. Female BALB/c mice (6 weeks; weight, 20 to 24 g) were kept under standard conditions with ad libitum food and water. On day 0, animals from the treatment group ($n = 7$) were first anesthetized with isoflurane. Then, an aseptic surgical site was prepared on the mice's lower abdomen followed by an incision of ~8 mm. The stent segment was implanted into the abdominal cavity and the incision was closed with suture. On day 4, another incision of ~8 mm was made, and the antibiofilm robot (0.2 g) was delivered through the incision to the inner of the stent, and actuated to release the antimicrobial (levofloxacin 250 μg/g) and remove the biofilm. After 5 min of treatment, the first robot was retrieved by a permanent magnet and another robot was delivered for treatment for another 5 min. Last, the second antibiofilm robot was retrieved and the incision was closed with suture. Blood samples were collected on days 7, 10, and 13, and the mice were weighed daily. For the control group ($n = 8$), the stent segment was implanted on day 0 and the surgical challenge was made on day 4 but no antibiofilm robot was applied. For the bacteria count on the stents after the antibiofilm treatment, the stents were removed from the animals on day 4 and immersed in PBS solution. The solutions were sonicated for 10 min, and the bacteria count was measured by the plate counting method.

Statistical analysis

Error bars represent the SD of three technical repeats unless otherwise specified. Two-tailed unpaired Student's t test was used to assess the statistical significance unless otherwise specified, where $P < 0.05$ is considered a significant difference.

Supplementary Materials

The PDF file includes:

Supplementary Text S1 to S3
Tables S1 to S4
Figs. S1 to S18
Legends for movies S1 to S8
References

Other Supplementary Material for this manuscript includes the following:

Movies S1 to S8

REFERENCES AND NOTES

1. Antimicrobial Resistance Collaborators, Global burden of bacterial antimicrobial resistance in 2019: A systematic analysis. *Lancet* **399**, 629–655 (2022).
2. V. Choi, J. L. Rohn, P. Stoodley, D. Carugo, E. Stride, Drug delivery strategies for antibiofilm therapy. *Nat. Rev. Microbiol.* **21**, 555–572 (2023).
3. H.-C. Flemming, J. Wingender, U. Szewzyk, P. Steinberg, S. A. Rice, S. Kjelleberg, Biofilms: An emergent form of bacterial life. *Nat. Rev. Microbiol.* **14**, 563–575 (2016).
4. K. Sauer, P. Stoodley, D. M. Goeres, L. Hall-Stoodley, M. Burmølle, P. S. Stewart, T. Bjarnsholt, The biofilm life cycle: Expanding the conceptual model of biofilm formation. *Nat. Rev. Microbiol.* **20**, 608–620 (2022).
5. H. C. Flemming, J. Wingender, The biofilm matrix. *Nat. Rev. Microbiol.* **8**, 623–633 (2010).
6. R. A. G. da Silva, I. Afonina, K. A. Kline, Eradicating biofilm infections: An update on current and prospective approaches. *Curr. Opin. Microbiol.* **63**, 117–125 (2021).
7. P. S. Stewart, J. W. Costerton, Antibiotic resistance of bacteria in biofilms. *Lancet* **358**, 135–138 (2001).
8. J. W. Costerton, P. S. Stewart, E. P. Greenberg, Bacterial biofilms: A common cause of persistent infections. *Science* **284**, 1318–1322 (1999).
9. C. R. Arciola, D. Campoccia, L. Montanaro, Implant infections: Adhesion, biofilm formation and immune evasion. *Nat. Rev. Microbiol.* **16**, 397–409 (2018).
10. H. Xie, M. Sun, X. Fan, Z. Lin, W. Chen, L. Wang, L. Dong, Q. He, Reconfigurable magnetic microrobot swarm: Multimode transformation, locomotion, and manipulation. *Sci. Robot.* **4**, eaav8006 (2019).
11. H. Xu, M. Medina-Sánchez, V. Magdanz, L. Schwarz, F. Hebenstreit, O. G. Schmidt, Sperm-hybrid micromotor for targeted drug delivery. *ACS Nano* **12**, 327–337 (2018).
12. X.-Z. Chen, B. Jang, D. Ahmed, C. Hu, C. De Marco, M. Hoop, F. Mushtaq, B. J. Nelson, S. Pané, Small-scale machines driven by external power sources. *Adv. Mater.* **30**, 1705061 (2018).
13. D. Ahmed, A. Sukhov, D. Hauri, D. Rodrigue, G. Maranta, J. Harting, B. J. Nelson, Bioinspired acousto-magnetic microswarm robots with upstream motility. *Nat. Mach. Intell.* **3**, 116–124 (2021).
14. J. Li, B. E. F. De Ávila, W. Gao, L. Zhang, J. Wang, Micro/nanorobots for biomedicine: Delivery, surgery, sensing, and detoxification. *Sci Robot* **2**, eaam6431 (2017).
15. B. J. Nelson, I. K. Kaliakatsos, J. J. Abbott, Microrobots for minimally invasive medicine. *Annu. Rev. Biomed. Eng.* **12**, 55–85 (2010).
16. G. Z. Yang, J. Bellingham, P. E. Dupont, P. Fischer, L. Floridi, R. Full, N. Jacobstein, V. Kumar, M. McNutt, R. Merrifield, B. J. Nelson, B. Scassellati, M. Taddeo, R. Taylor, M. Veloso, Z. L. Wang, R. Wood, The grand challenges of science robotics. *Sci Robot* **3**, eaar7650 (2018).
17. G. Z. Yang, B. J. Nelson, R. R. Murphy, H. Choset, H. Christensen, S. H. Collins, P. Dario, K. Goldberg, K. Ikuta, N. Jacobstein, D. Kragic, R. H. Taylor, M. McNutt, Combating COVID-19—The role of robotics in managing public health and infectious diseases. *Sci Robot* **5**, eabb5589 (2020).
18. B. J. Nelson, S. Gervasoni, P. W. Y. Chiu, L. Zhang, A. Zemmar, Magnetically actuated medical robots: An in vivo perspective. *Proc. IEEE* **110**, 1028–1037 (2022).
19. J. Li, C. C. Mayorga-Martinez, C.-D. Ohl, M. Pumera, J. Li, C. C. Mayorga-Martinez, M. Pumera, C.-D. Ohl, Ultrasonically propelled micro- and nanorobots. *Adv. Funct. Mater.* **32**, 2102265 (2022).
20. L. Xu, F. Mou, H. Gong, M. Luo, J. Guan, Light-driven micro/nanomotors: From fundamentals to applications. *Chem. Soc. Rev.* **46**, 6905–6926 (2017).
21. Q. Wang, Q. Wang, Z. Ning, K. F. Chan, J. Jiang, Y. Wang, L. Su, S. Jiang, B. Wang, B. Y. M. Ip, H. Ko, T. W. H. Leung, P. W. Y. Chiu, S. C. H. Yu, L. Zhang, Tracking and navigation of a microswarm under laser speckle contrast imaging for targeted delivery. *Sci. Robot.* **9**, eadh1978 (2024).
22. Q. Wang, X. Du, D. Jin, L. Zhang, Real-time ultrasound doppler tracking and autonomous navigation of a miniature helical robot for accelerating thrombolysis in dynamic blood flow. *ACS Nano* **16**, 604–616 (2022).
23. B. J. Nelson, S. Pané, Delivering drugs with microrobots. *Science* **382**, 1120–1122 (2023).
24. J. Yoo, S. Tang, W. Gao, Micro- and nanorobots for biomedical applications in the brain. *Nat. Rev. Bioeng.* **1**, 308–310 (2023).
25. B. Sun, S. Kjelleberg, J. J. Y. Sung, L. Zhang, Micro- and nanorobots for biofilm eradication. *Nat. Rev. Bioeng.* **2**, 367–369 (2024).
26. H. H. Tran, A. Watkins, M. J. Oh, A. Babeer, T. P. Schaer, E. Steager, H. Koo, Targeting biofilm infections in humans using small scale robotics. *Trends Biotechnol.* **42**, 479–495 (2024).
27. C. C. Mayorga-Martinez, L. Zhang, M. Pumera, Chemical multiscale robotics for bacterial biofilm treatment. *Chem. Soc. Rev.* **53**, 2284–2299 (2024).
28. A. Elbourne, S. Cheeseman, P. Atkin, N. P. Truong, N. Syed, A. Zavabeti, M. Mohiuddin, D. Esrafilzadeh, D. Cozzolino, C. F. McConville, M. D. Dickey, R. J. Crawford, K. Kalantar-Zadeh, J. Chapman, T. Daeneke, V. K. Truong, Antibacterial liquid metals: Biofilm treatment via magnetic activation. *ACS Nano* **14**, 802–817 (2020).
29. W. Wang, J. V. I. Timonen, A. Carlson, D. M. Drotlef, C. T. Zhang, S. Kolle, A. Grinthal, T. S. Wong, B. Hatton, S. H. Kang, S. Kennedy, J. Chi, R. T. Blough, M. Sitti, L. Mahadevan, J. Aizenberg, Multifunctional ferrofluid-infused surfaces with reconfigurable multiscale topography. *Nature* **559**, 77–82 (2018).
30. G. Hwang, A. J. Paula, E. E. Hunter, Y. Liu, A. Babeer, B. Karabucak, K. Stebe, V. Kumar, E. Steager, H. Koo, Catalytic antimicrobial robots for biofilm eradication. *Sci. Robot.* **4**, eaaw2388 (2019).
31. M. J. Oh, A. Babeer, Y. Liu, Z. Ren, J. Wu, D. A. Issadore, K. J. Stebe, D. Lee, E. Steager, H. Koo, Surface topography-adaptive robotic superstructures for biofilm removal and pathogen detection on human teeth. *ACS Nano* **16**, 11998–12012 (2022).
32. Y. Dong, L. Wang, K. Yuan, F. Ji, J. Gao, Z. Zhang, X. Du, Y. Tian, Q. Wang, L. Zhang, Magnetic microswarm composed of porous nanocatalysts for targeted elimination of biofilm occlusion. *ACS Nano* **15**, 5056–5067 (2021).
33. K. Villa, J. Viktorova, J. Plutnar, T. Ruml, L. Hoang, M. Pumera, Chemical microrobots as self-propelled microbrushes against dental biofilm. *Cell Rep. Phys. Sci.* **1**, 100181 (2020).
34. M. Ussia, M. Urso, K. Dolezelikova, H. Michalkova, V. Adam, M. Pumera, Active light-powered antibiofilm ZnO micromotors with chemically programmable properties. *Adv. Funct. Mater.* **31**, 2101178 (2021).
35. M. Ussia, M. Urso, S. Kment, T. Fialova, K. Klima, K. Dolezelikova, M. Pumera, Light-propelled nanorobots for facial titanium implants biofilms removal. *Small* **18**, e2200708 (2022).
36. C. C. Mayorga-Martinez, J. Zelenka, K. Klima, P. Mayorga-Burrezo, L. Hoang, T. Ruml, M. Pumera, Swarming magnetic photoactive microrobots for dental implant biofilm eradication. *ACS Nano* **16**, 8694–8703 (2022).
37. B. Sun, M. Sun, Z. Zhang, Y. Jiang, B. Hao, X. Wang, Y. Cao, T. K. F. Chan, L. Zhang, Magnetic hydrogel micromachines with active release of antibacterial agent for biofilm eradication. *Adv. Intell. Syst.* **6**, 2300092 (2024).

38. V. Milosavljevic, L. Kosaristanova, K. Dolezelikova, V. Adam, M. Pumera, V. Milosavljevic, M. Pumera, K. Dolezelikova, V. Adam, Microrobots with antimicrobial peptide nanoarchitectonics for the eradication of antibiotic-resistant biofilms. *Adv. Funct. Mater.* **32**, 2112935 (2022).
39. C. C. Mayorga-Martinez, J. Zelenka, K. Klima, M. Kubanova, T. Ruml, M. Pumera, Multimodal-driven magnetic microrobots with enhanced bactericidal activity for biofilm eradication and removal from titanium mesh. *Adv. Mater.* **35**, e2300191 (2023).
40. Y. Dong, L. Wang, Z. Zhang, F. Ji, T. K. F. Chan, H. Yang, C. P. L. Chan, Z. Yang, Z. Chen, W. T. Chang, J. Y. K. Chan, J. J. Y. Sung, L. Zhang, Endoscope-assisted magnetic helical micromachine delivery for biofilm eradication in tympanostomy tube. *Sci. Adv.* **8**, eabq8573 (2022).
41. M. Sun, K. F. Chan, Z. Zhang, L. Wang, Q. Wang, S. Yang, S. M. Chan, P. W. Y. Chiu, J. J. Y. Sung, L. Zhang, Magnetic microswarm and fluoroscopy-guided platform for biofilm eradication in biliary stents. *Adv. Mater.* **34**, e2201888 (2022).
42. P. I. Baburova, D. V. Kladko, A. Lokteva, A. Pozhitkova, V. Rumyantceva, V. Rumyantceva, I. V. Pankov, S. Taskaev, V. V. Vinogradov, Magnetic soft robot for minimally invasive urethral catheter biofilm eradication. *ACS Nano* **17**, 20925–20938 (2023).
43. M. Sitti, D. S. Wiersma, Pros and cons: Magnetic versus optical microrobots. *Adv. Mater.* **32**, e1906766 (2020).
44. G. Cai, J. Wang, K. Qian, J. Chen, S. Li, P. See Lee, Extremely stretchable strain sensors based on conductive self-healing dynamic cross-links hydrogels for human-motion detection. *Adv. Sci.* **4**, 1600190 (2017).
45. M. Sun, C. Tian, L. Mao, X. Meng, X. Shen, B. Hao, X. Wang, H. Xie, L. Zhang, Reconfigurable magnetic slime robot: Deformation, adaptability, and multifunction. *Adv. Funct. Mater.* **32**, 2112508 (2022).
46. W. L. A. Brooks, B. S. Sumerlin, Synthesis and applications of boronic acid-containing polymers: From materials to medicine. *Chem. Rev.* **116**, 1375–1397 (2016).
47. M. Chen, Y. Wu, B. Chen, A. M. Tucker, A. Jagota, S. Yang, Fast, strong, and reversible adhesives with dynamic covalent bonds for potential use in wound dressing. *Proc. Natl. Acad. Sci. U.S.A.* **119**, e2203074119 (2022).
48. Y. Feng, C. Wu, M. Chen, H. Sun, A. Lenus, R. Vellaisamy, W. A. Daoud, X. Yu, G. Zhang, W. J. Li, Amoeba-inspired self-healing electronic slime for adaptable, durable epidermal wearable electronics. *Adv. Funct. Mater.* **34**, 2402393 (2024).
49. Y. Kim, X. Zhao, Magnetic soft materials and robots. *Chem. Rev.* **122**, 5317–5364 (2022).
50. R. Zhao, Y. Kim, S. A. Chester, P. Sharma, X. Zhao, Mechanics of hard-magnetic soft materials. *J. Mech. Phys. Solids* **124**, 244–263 (2019).
51. G. Dong, Q. He, S. Cai, Magnetic vitrimer-based soft robotics. *Soft Matter* **18**, 7604–7611 (2022).
52. J. Yu, D. Jin, K. F. Chan, Q. Wang, K. Yuan, L. Zhang, Active generation and magnetic actuation of microrobotic swarms in bio-fluids. *Nat. Commun.* **10**, 5631 (2019).
53. L. Yang, J. Jiang, X. Gao, Q. Wang, Q. Dou, L. Zhang, Autonomous environment-adaptive microrobot swarm navigation enabled by deep learning-based real-time distribution planning. *Nat. Mach. Intell.* **4**, 480–493 (2022).
54. M. Sun, S. Yang, J. Jiang, S. Jiang, M. Sitti, L. Zhang, Bioinspired self-assembled colloidal collectives drifting in three dimensions underwater. *Sci. Adv.* **9**, eadj4201 (2023).
55. Y. Xiang, J. Zhang, A theoretical investigation of the ability of magnetic miniature robots to exert forces and torques for biomedical functionalities. *IEEE Robot Autom Lett* **8**, 1771–1777 (2023).
56. S. Aggarwal, R. M. Hozalski, Determination of biofilm mechanical properties from tensile tests performed using a micro-cantilever method. *Biofouling* **26**, 479–486 (2010).
57. H. Boudarel, J. D. Mathias, B. Blaysat, M. Grédiac, Towards standardized mechanical characterization of microbial biofilms: Analysis and critical review. *NPJ Biofilms Microbiomes* **4**, 17 (2018).
58. J. Peng, S. Xie, K. Huang, P. Ran, J. Wei, Z. Zhang, X. Li, Nitric oxide-propelled nanomotors for bacterial biofilm elimination and endotoxin removal to treat infected burn wounds. *J. Mater. Chem. B* **10**, 4189–4202 (2022).
59. B. Lu, E. Hu, R. Xie, K. Yu, F. Lu, R. Bao, C. Wang, G. Lan, F. Dai, Magnetically guided nanoworms for precise delivery to enhance in situ production of nitric oxide to combat focal bacterial infection in vivo. *ACS Appl. Mater. Interfaces* **13**, 22225–22239 (2021).
60. T. Cui, S. Wu, Y. Sun, J. Ren, X. Qu, Self-propelled active photothermal nanoswimmer for deep-layered elimination of biofilm in vivo. *Nano Lett.* **20**, 7350–7358 (2020).
61. A. Galstyan, R. Schiller, U. Dobrindt, Boronic acid functionalized photosensitizers: A strategy to target the surface of bacteria and implement active agents in polymer coatings. *Angew. Chem. Int. Ed. Engl.* **56**, 10362–10366 (2017).
62. X. Yang, W. Shang, H. Lu, Y. Liu, L. Yang, R. Tan, X. Wu, Y. Shen, An agglutinate magnetic spray transforms inanimate objects into millirobots for biomedical applications. *Sci. Robot.* **5**, eabc8191 (2020).
63. R. B. Wilson, Y. Farooque, Risks and prevention of surgical site infection after hernia mesh repair and the predictive utility of ACS-NSQIP. *J. Gastrointest. Surg.* **26**, 950–964 (2022).
64. B. Pérez-Köhler, F. García-Moreno, T. Brune, G. Pascual, J. M. Bellón, Preclinical bioassay of a polypropylene mesh for hernia repair pretreated with antibacterial solutions of chlorhexidine and allicin: An in vivo study. *PLOS ONE* **10**, e0142768 (2015).
65. J. Y. Sung, J. W. C. Leung, E. A. Shaffer, K. Lam, J. W. Costerton, Bacterial biofilm, brown pigment stone and blockage of biliary stents. *J. Gastroenterol. Hepatol.* **8**, 28–34 (1993).
66. A. Chauhan, J. M. Ghigo, C. Beloin, Study of in vivo catheter biofilm infections using pediatric central venous catheter implanted in rat. *Nat. Protoc.* **11**, 525–541 (2016).
67. C. C. Deng, W. L. A. Brooks, K. A. Abboud, B. S. Sumerlin, Boronic acid-based hydrogels undergo self-healing at neutral and acidic pH. *ACS Macro Lett.* **4**, 220–224 (2015).
68. L. M. C. Collins, C. Dawes, The surface area of the adult human mouth and thickness of the salivary film covering the teeth and oral mucosa. *J. Dent. Res.* **66**, 1300–1302 (1987).
69. B. Sun, R. Jia, H. Yang, X. Chen, K. Tan, Q. Deng, J. Tang, Magnetic arthropod millirobots fabricated by 3D-printed hydrogels. *Adv. Intell. Syst.* **4**, 2100139 (2022).
70. R. Zhang, S. Wu, Q. Ze, R. Zhao, Micromechanics study on actuation efficiency of hard-magnetic soft active materials. *J. Appl. Mech.* **87**, 091008 (2020).
71. E. S. Gloag, S. Fabbri, D. J. Wozniak, P. Stoodley, Biofilm mechanics: Implications in infection and survival. *Biofilm* **2**, 100017 (2020).
72. T. Bjarnsholt, M. Alhede, M. Alhede, S. R. Eickhardt-Sørensen, C. Moser, M. Kühl, P. Ø. Jensen, N. Høiby, The in vivo biofilm. *Trends Microbiol.* **21**, 466–474 (2013).
73. D. Ershov, M. S. Phan, J. W. Pylvänäinen, S. U. Rigaud, L. Le Blanc, A. Charles-Orszag, J. R. W. Conway, R. F. Laine, N. H. Roy, D. Bonazzi, G. Duménil, G. Jacquemet, J. Y. Tinevez, TrackMate 7: Integrating state-of-the-art segmentation algorithms into tracking pipelines. *Nat. Methods* **19**, 829–832 (2022).
74. N. Tarantino, J. Y. Tinevez, E. F. Crowell, B. Boisson, R. Henriques, M. Mhlanga, F. Agou, A. Israël, E. Laplantine, Tnf and il-1 exhibit distinct ubiquitin requirements for inducing NEMO-IKK supramolecular structures. *J. Cell Biol.* **204**, 231–245 (2014).
75. A. Birjiniuk, N. Billings, E. Nance, J. Hanes, K. Ribbeck, P. S. Doyle, Single particle tracking reveals spatial and dynamic organization of the *Escherichia coli* biofilm matrix. *New J. Phys.* **16**, 085014 (2014).

Acknowledgments: We thank X. Wang from the Mechanical and Automation Engineering Department, CUHK for the help in SEM characterization. We also thank the support from the CUHK International Joint Supervision of PhD Students Scheme; the Multi-scale Medical Robotics Centre (MRC), InnoHK, at the Hong Kong Science Park; and the SIAT-CUHK Joint Laboratory of Robotics and Intelligent Systems. Some of the schematics (Figs. 1B, 4, A and E, and 5C) used pictures from Servier Medical Art as material under the Creative Common Attribution 4.0 license: http://creativecommons.org/licenses/by/4.0/. **Funding:** This work was supported by Hong Kong Research Grants Council grant R4015-21 (L.Z.), Hong Kong Research Grants Council grant RFS2122-4S03 (L.Z.), Hong Kong Research Grants Council Collaborative Research Fund C1134-20GF (L.Z.), Croucher Foundation Grant CAS20403 (L.Z.), and CUHK internal grants (L.Z.).
Author contributions: Conceptualization: B.S., M.S., J.J.Y.S., and L.Z. Methodology: B.S., T.K.F.C., and M.S. Investigation: B.S., J.G., B.H., Y.C., T.K.F.C., and M.S. Visualization: B.S. Supervision: M.S., J.J.Y.S., and L.Z. Writing—original draft: B.S. and M.S. Writing—review and editing: J.G., T.K.F.C., M.S., J.J.Y.S., and L.Z. **Competing interests:** The authors declare that they have no competing interests. **Data and materials availability:** All data needed to evaluate the conclusions in the paper are present in the paper and/or the Supplementary Materials.

Submitted 12 October 2024
Accepted 5 February 2025
Published 12 March 2025
10.1126/sciadv.adt8213